
REALISTIC DUNE FIELD SURFACE STRESS PREDICTION (TECHNICAL REPORT)

A PREPRINT

Chao Wang, Ph.D.

The University of Texas at Dallas
Richardson, TX
cxw151530@utdallas.edu

October 26, 2021

ABSTRACT

The dune morphodynamics study is under highly focused recently, due to aeolian process induced nonlinear correlation to sediment modification over bedform. Surface stress, inflicted by aloft upcoming wind, impacts, crucially, the sediment erosion pattern. The aloft atmospheric dune surface layer (ASL) is composed of inertial layer and roughness sublayer. The logarithmic velocity profile is valid within inertial layer based on previous findings, where attached-eddy occupied the higher elevations scaled with local wall-normal height (Wang and Anderson, 2019a). While, mixing layer velocity profile is displayed in this work to predict the surface shear over White Sands National Monument (WSNM), the length scale of which is revealed as proportional to mixing layer length scale. Given the realistic dune field morphology and aeolian process, a series of mathematic stress models have been proposed and verified. Among these models, mixing layer model shows the best performance, which elucidates and confirms the mixing layer analogy over realistic dune field. Finally, a schematic structural model shows that “sediment scour” and “flow channeling” indeed is the reason for the large residual values distributed in narrow interdune surfaces, which has a great consistency with previous finding (Wang and Anderson, 2018b).

1 Large-Eddy Simulation & Cases

Recently, Computational Fluid Dynamics (CFD) method benefits a wide range of researches such as biomedicine, environment, geoscience and so forth, wherein different length scales of fluid are involved in these CFD simulations, especially in turbulent flow which consisted of a broad range of spectrum (Wang, 2019). To recover the geophysical fluid field, Direct Numerical Simulation (DNS) could be a promising methodology, resolving turbulence from Kolmogorov scale to the maximum of numerical length scale (Pope, 2000). However, DNS is too “expensive” for most geophysical fluid simulations due to the critical computational resource need in high Reynolds number flow regime. In contrast, LES can approach highly credible results with an acceptable numerical requirement (Metias, 1964). In this chapter, Large-Eddy Simulation method will be detailed discussed. Meanwhile, in Section 1.2, all numerical cases details will be provided.

1.1 Large-Eddy Simulation

In Large-Eddy Simulation (LES) method, the filtered three-dimensional transport equation, incompressible momentum,

$$D_t \tilde{\mathbf{u}}(\mathbf{x}, t) = \rho^{-1} \mathbf{F}(\mathbf{x}, t), \quad (1)$$

is solved, where ρ is density, $\tilde{\cdot}$ denotes a grid-filtered quantity, $\mathbf{u}(\mathbf{x}, t)$ is velocity (in this work, u, v, w are corresponded to velocity in streamwise, spanwise and wall-normal direction, respectively) and $\mathbf{F}(\mathbf{x}, t)$ is the collection of forces (pressure correction, pressure gradient, stress heterogeneity and obstacle forces). The grid-filtering operation is attained

here via convolution with the spatial filtering kernel, $\tilde{\mathbf{u}}(\mathbf{x}, t) = G_\Delta \star \mathbf{u}(\mathbf{x}, t)$, or in the following form

$$\tilde{\mathbf{u}}(\mathbf{x}, t) = \oint G_\Delta(\mathbf{x} - \mathbf{x}', t) \mathbf{u}(\mathbf{x}', t) d\mathbf{x}', \quad (2)$$

where Δ is the filter scale (Meneveau and Katz, 2000). A right-hand side forcing term, $-\nabla \cdot \mathbf{T}$, will be generated after the filtering operation to momentum equation, where $\mathbf{T} = \langle \mathbf{u}' \otimes \mathbf{u}' \rangle_t$ is the subgrid-scale stress tensor and $\langle \cdot \rangle_a$ denotes averaging over dimension, a (in this article, rank-1 and -2 tensors are denoted with bold-italic and bold-sans relief, respectively).

For the present study, $D_t \tilde{\mathbf{u}}(\mathbf{x}, t) = \rho^{-1} \mathbf{F}(\mathbf{x}, t)$ is solved for a channel-flow arrangement (Albertson and Parlange, 1999; Anderson and Chamecki, 2014), with the flow forced by a pressure gradient in streamwise direction, $\mathbf{\Pi} = \{\Pi, 0, 0\}$, where

$$\Pi = [dP_0/dx] \frac{H}{\rho} = \tau^w / \rho = u_*^2 = 1, \quad (3)$$

which sets the shear velocity, u_* , upon which all velocities are non-dimensionalized. In simulation, all length scales are normalized by H , which is the surface layer depth, and velocity are normalized by surface shear velocity. $D_t \tilde{\mathbf{u}}(\mathbf{x}, t) = \rho^{-1} \mathbf{F}(\mathbf{x}, t)$ is solved for high-Reynolds number, fully-rough conditions (Jimenez, 2004), and thus viscous effects can be neglected in simulation, $\nu \nabla^2 \tilde{\mathbf{u}}(\mathbf{x}, t) = 0$. Under the presumption of $\rho(\mathbf{x}, t) \rightarrow \rho$, the velocity vector is solenoidal, $\nabla \cdot \tilde{\mathbf{u}}(\mathbf{x}, t) = 0$. During LES, the (dynamic) pressure needed to preserve $\nabla \cdot \tilde{\mathbf{u}}(\mathbf{x}, t) = 0$ is dynamically computed by computation of $\nabla \cdot [D_t \tilde{\mathbf{u}}(\mathbf{x}, t) = \rho^{-1} \mathbf{F}(\mathbf{x}, t)]$ and imposing $\nabla \cdot \tilde{\mathbf{u}}(\mathbf{x}, t) = 0$, which yields a resultant pressure Poisson equation.

The channel-flow configuration is created by the aforementioned pressure-gradient forcing, and the following boundary condition prescription: at the domain top, the zero-stress Neumann boundary condition is imposed on streamwise and spanwise velocity, $\partial \tilde{u} / \partial z|_{z/H=1} = \partial \tilde{v} / \partial z|_{z/H=1} = 0$. The zero vertical velocity condition is imposed at the domain top and bottom, $\tilde{w}(x, y, z/H = 0) = \tilde{w}(x, y, z/H = 1) = 0$. Spectral discretization is used in the horizontal directions, thus imposing periodic boundary conditions on the vertical “faces” of the domain, *vis*.

$$\phi(x + mL_x, y + nL_y, z) = \phi(x, y, z), \quad (4)$$

and imposing spatial homogeneity in the horizontal dimensions. The code uses a staggered-grid formulation (Albertson and Parlange, 1999), where the first grid points for $\tilde{u}(\mathbf{x}, t)$ and $\tilde{v}(\mathbf{x}, t)$ are located at $\delta z/2$, where $\delta z = H/N_z$ is the resolution of the computational mesh in the vertical (N_z is the number of vertical grid points). Grid resolution in the streamwise and spanwise direction is $\delta x = L_x/N_x$ and $\delta y = L_y/N_y$, respectively, where L and N denote horizontal domain extent and corresponding number of grid points (subscript x or y denotes streamwise or spanwise direction, respectively). Table 1 provides a summary of the domain attributes for the different cases, where the domain height has been set to the depth of the surface layer, $L_z/H = 1$.

At the lower boundary, surface momentum fluxes are prescribed with a hybrid scheme leveraging an immersed-boundary method (IBM)(Anderson and Meneveau, 2010; Anderson, 2012) and the equilibrium logarithmic model (Piomelli and Balaras, 2002), depending on the digital elevation map, $h(x, y)$. When $h(x, y) < \delta z/2$, the topography vertically unresolved, and the logarithmic law is used:

$$\tau_{xz}^w(x, y, t) = - \left[\frac{\kappa U(x, y, t)}{\log(\frac{1}{2} \delta z / \hat{z}_0)} \right]^2 \frac{\tilde{u}(x, y, \frac{1}{2} \delta z, t)}{U(x, y, t)} \quad (5)$$

and

$$\tau_{yz}^w(x, y, t) = - \left[\frac{\kappa U(x, y, t)}{\log(\frac{1}{2} \delta z / \hat{z}_0)} \right]^2 \frac{\tilde{v}(x, y, \frac{1}{2} \delta z, t)}{U(x, y, t)} \quad (6)$$

where $\hat{z}_0/H = 2 \times 10^{-4}$ is a prescribed roughness length, $\tilde{\cdot}$ denotes test-filtering (Germano, 1992; Germano et al., 1991) (used here to attenuate un-physical local surface stress fluctuations associated with localized application of Equation 5 and 6 (Bou-Zeid et al., 2005)), and $U(x, y, \frac{1}{2} \delta z, t) = (\tilde{u}(x, y, \frac{1}{2} \delta z, t)^2 + \tilde{v}(x, y, \frac{1}{2} \delta z, t)^2)^{1/2}$ is magnitude of the test-filtered velocity vector. Where $h(x, y) > \frac{1}{2} \delta z$, a continuous forcing Iboldsymbol is used (Anderson, 2012; Mittal and Iaccarino, 2005), which has been successfully used in similar studies of turbulent obstructed shear flows (Anderson and Chamecki, 2014; Anderson et al., 2015; Anderson, 2016). The immersed boundary method computes a body force, which imposes circumferential momentum fluxes at computational “cut” cells based on spatial gradients of $h(x, y)$:

$$\mathbf{f}(\mathbf{x}, t) = - \frac{\tilde{\mathbf{u}}(\mathbf{x}, t)}{\delta z} R(\tilde{\mathbf{u}}(\mathbf{x}, t) \cdot \nabla h), \quad (7)$$

where R is called Ramp Function (Anderson, 2012)

$$R(x) = \begin{cases} x & \text{for } x > 0, \\ 0 & \text{for } x \leq 0. \end{cases} \quad (8)$$

Equations 5 and 6 are needed to ensure surface stress is imposed when $h(x, y) < \frac{1}{2}\delta z$. Subgrid-scale stresses are modeled with an eddy-viscosity model,

$$\boldsymbol{\tau}^d = -2\nu_t \mathbf{S}, \quad (9)$$

where

$$\mathbf{S} = \frac{1}{2}(\nabla \tilde{\mathbf{u}} + \nabla \tilde{\mathbf{u}}^T) \quad (10)$$

is the resolved strain-rate tensor. The eddy viscosity is

$$\nu_t = (C_s \Delta)^2 |\mathbf{S}|, \quad (11)$$

where $|\mathbf{S}| = (2\mathbf{S} : \mathbf{S})^{1/2}$, C_s is the Smagorinsky coefficient, and Δ is the grid resolution. For the present simulations, the Lagrangian scale-dependent dynamic model is used (Bou-Zeid et al., 2005). The simulations have been run for $N_t \delta_t U_0 u_{*,d} H^{-1} \approx 10^3$ large-eddy turnovers, where $U_0 = \langle \tilde{u}(x, y, (L_z - \delta z/2)/H = 1, t) \rangle_t$ is a “free stream” or centerline velocity. This duration is sufficient for computation of Reynolds-averaged quantities.

1.2 Cases

The White Sands National Monument (WSNM) dune field is located in the Tularosa Basin of the Rio Grande Rift, between the San Andres and Sacramento Mountain Ranges, in southern New Mexico. The WSNM dune field consists of a core of barchan dunes, which abruptly transition to parabolic dunes (Ewing and Kocurek, 2010a,b; Jerolmack and Mohrig, 2005). Recently, the increasing trend of aerodynamic roughness of dune field in the upcoming wind direction has been imputed to the developing of the internal momentum boundary layer (Jerolmack and Mohrig, 2005). The WSNM DEM is taken from an existing LiDAR survey. (Anderson and Chamecki, 2014) has chosen a series windows of WSNM DEM and analyzed DFSL which depicts profound turbulence enveloped beneath shear layers for elevation less than two to three times the dune crest height. For a comprehensive understanding of the turbulence coherence in DFSL, a portion of WSNM DEM has been chosen for this study. Figure 5 (b) displays the subset area of WSNM used as a lower boundary during LES. In terms of geometric complexity, the DEM serves as an ‘upper limit’ with its multiscale distribution of dune sizes and shapes. Importantly, the feature of WSNM reveal the most common and typical dune field which includes overlapping and collision with adjacent dunes, which confounds efforts to isolate universal flow pattern.

Two *a priori* modifications are imposed on the chosen DEM: (i) the lowest elevation is subtracted from the DEM, which imposes the minimum elevation of DEM is 0, $\min(h(\mathbf{x})) = 0$; (ii) a two-dimensionl windowing function $\mathcal{W}(x, y) = a(x)a(y)$ to the resulting topography in order to impose periodicity on the underlying topography $h(x, y)$. Hence, the modified topography is the Hadamard product $h(x, y) \Rightarrow h(x, y)\mathcal{W}(x, y)$. Periodicity is needed due to the use of spectral decomposition of flow quantities in LES. The Gibbs phenomena will contaminate the results if $h(x, y)$ is not periodic (Tseng et al., 2006). The windowing function is in the following format:

$$a(x) = \begin{cases} 1.0 & \text{for } 0 \leq \|x - x_c\| < \gamma L, \\ \cos \left[\frac{(x - x_c)/H - \gamma(L/H)}{2(1-\gamma)} \right] & \text{for } \gamma L \leq \|x - x_c\| < L, \end{cases} \quad (12)$$

where L is the length of simulation domain ($L = 1000m$ in this work), H is the simulation characteristic length scale to normalize all lengths ($H = 100m$ in this work, which is sufficient to recover dune roughness sublayer and inertial sublayer). The parameter γ imposes the circumjacent width over which the topography around the edges of the focus area is forced toward $h(x, y) = 0$, and x_c is the coordinate of the center of the domain. In the present study, we select $\gamma = 0.85$, which imposes that the outermost 15% of $h(x, y)$ gradually tends toward zero (see Figure 1 (a)).

Figure 1 (a) displays the White Sands National Monument (WSNM) DEM. Figure 1 (b) captured the brinklines of WSNM via

$$\frac{\partial h}{\partial x} \approx 0. \quad (13)$$

The interactive collision is evident in realistic dune field, associated with red lines tangling with each other. From brinkline map, the length scale of brinkline is much larger than the dune height, where the maximum can be over hundred times the crest height. The meandering brinkline pattern is induced by the local non-uniformity of wind regime such as wind direction, velocity magnitude etc. In the following chapter, we will develop a series of stress model, given the known aeolian process models over dune fields, and assess the verification of each model through residual value calculating practices.

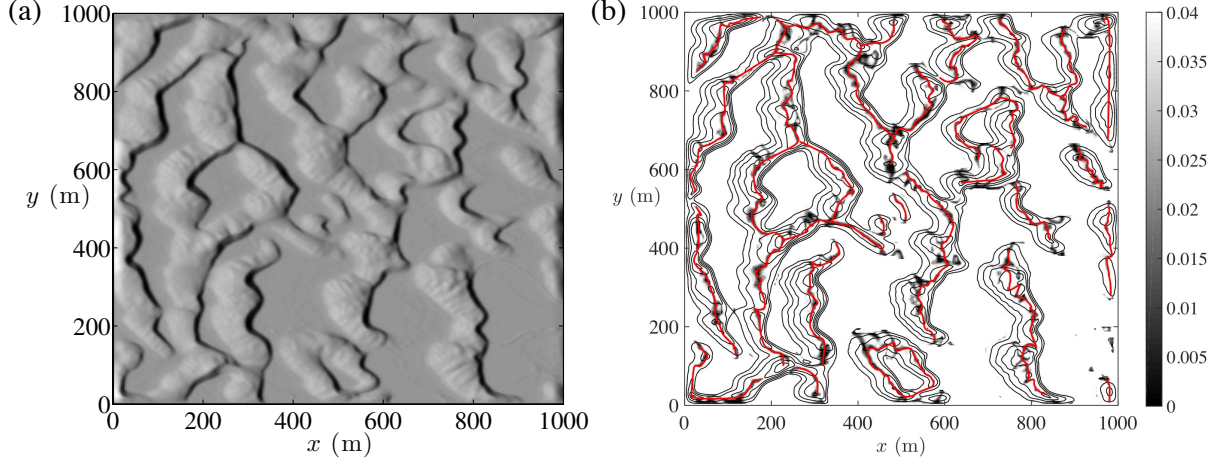


Figure 1: Panel (a) is White Sand National Monument Digital Elevation Model (DEM). Solar lighting has been included to highlight the dune field geometry, wherein light gray indicates stoss side, and dark gray indicates lee side. Based on Panel (a), the dune brinklines are captured based on equation 13 in Panel (b). The red line marks dune field ridges. The black area indicates $\partial h / \partial x \approx 0$ area.

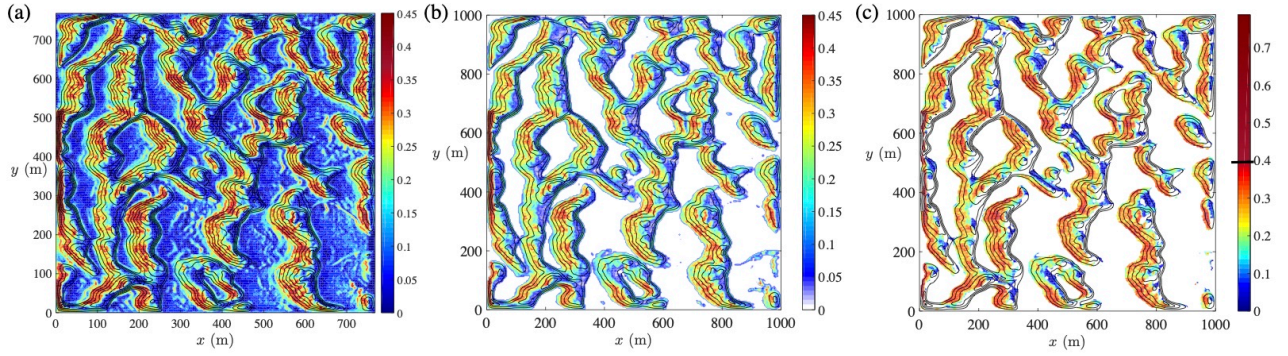


Figure 2: Surface shear stress magnitude are captured through Immersed Boundary Method (IBM) 7. Panel (a) displays the original surface shear stress distribution. Panel (b) is surface shear stress on dunes which excludes the values on walls. Based on Equation 10, the author prepared Panel (c) which exhibits the surface shear stress on windward face. Solid black line on colorbar of Panel (c) indicates the average value of high stress region.

2 Results

Surface shear stress magnitude over White Sands National Monument has been displayed in Figure 2. The stress magnitude is calculated via IBM (Eq.7) (Anderson, 2012). Panel (a) shows the surface shear stress magnitude. The shear stress $\tau_{w,0}(\mathbf{x})$ is normalized by the global friction velocity $\tau_w(\mathbf{x}) = \tau_{w,0}(\mathbf{x}) / u_{*,d}^2$. From Panel (a), we can see the high stress area is on the dune field windward faces. Meanwhile, with the wall-normal elevation increasing, the stress magnitude is enhanced. To elucidate the aeolian stress over dune surface, Panel (b) shows surface shear stress on dunes which excludes the values on walls, $\tau_w(x, y, z/h_w > 0)$. Panel (c) highlights the windward area stress via $\tau_w(\mathbf{x})S(\mathbf{x})$, where

$$S(\mathbf{x}) = \begin{cases} 0 & \text{for } \frac{\partial h}{\partial x} < 0, \\ 1 & \text{for } \frac{\partial h}{\partial x} > 0. \end{cases} \quad (14)$$

In general, the leeward stress magnitude is less than 0.1. In Panel (c), solid black line on colorbar highlights the critical magnitude on stoss side, $\tau_w > 0.4$. However, the high stress value can also be captured in some leeward faces and the areas where “flow-channeling” appears (Wang and Anderson, 2017; Wang et al., 2017; Wang and Anderson, 2018a,b, 2019a,b; Wang, 2019).

Table 1: Dune surface shear stress mathematic model β and average residual value, where $h(x)$ is dune field wall-normal elevation, L_s is shear length $L_s \approx h_{max}$, h_a is inflection height $h_a = 3h_{max}/4$, h_{max} is the maximum value of dune height.

β_n	γ_n	ξ_t (Eq18)
$\beta_0 = \beta$	$\gamma_0 = 1.0$	0.20
$\beta_1 = \beta\gamma_1$	$\gamma_1 = h(x, y)/h_{max}$	0.15
$\beta_2 = \beta\gamma_2$	$\gamma_2 = \sin(h\pi/2h_{max})$	0.15
$\beta_3 = \beta\gamma_3$	$\gamma_3 = \tan(h\pi/(2h_{max} \cdot k))$	0.17
$\beta_4 = \beta\gamma_4$	$\gamma_4 = \tan\left(\frac{h\pi}{2h_{max}} - k\right) + m$	0.29
$\beta_5 = \beta\gamma_5$	$\gamma_5 = \tanh\left[1 - \left(\frac{\frac{h}{h_{max}} - h_a}{L_s}\right)^2\right]$	0.15
$\beta_6 = \beta\gamma_6$	$\gamma_6 = 1 - \tanh^2\left(\frac{h-h_a}{L_s}\right)$	0.17
$\beta_7 = \beta\gamma_7$	$\gamma_7 = 1 + \tanh\left(\frac{h-h_a}{L_s}\right)$	0.15

In this work, several mathematical models have been proposed to capture the real dune field stress. To achieve that goal, the aeolian stress distribution over dune field should be understood first. Previously, Anderson and Chamecki (2014) has revealed the Kelvin-Helmholtz effect in White Sands National Monument dune field, where the spanwise vortex rollers shed from the previous dune crestline and propagate in downwelling. The structural model of mixing layer flow in aeolian crescentic dune field sublayer has been proposed in (Anderson and Chamecki, 2014), wherein the shear length L_s is observed though LES results, which is in half length scale of the vortex thickness, $L_s = 0.5\delta_\omega$. Wang and Anderson (2019a) has revealed the mixing-layer analogy in WSNM, where the vortex thickness is scaled with interdune mixing layer eddies, $\delta_\omega \sim L_\omega$. This is important, because it helps us to understand the role of turbulence played in this problem. That is the secondary flow induced by streamwise obstructive effects enhances the aeolian sediment erosion. Thus, high scaled turbulence correlation associated with logarithmic upcoming wind profile unavoidably makes local wall-normal elevation become a significant variable to predict surface stress. However, the nonlinear correlation between vertical elevation and second order statistics induces several following mathematic models to capture surface stresses. Due to the low stress magnitude in leeward faces, the following practices are focussing on stoss side stress analysis.

From the numerical analysis of surface stress, the stress magnitude displays a pseudo-linear correlation with dune stoss side gradient. Given the realistic dune morphologies, β has been adopted to present streamwise and transversal gradient effects, where

$$\beta(x) = \sqrt{\left[\frac{\partial h}{\partial x}\right]^2 + \left[\frac{\partial h}{\partial y}\right]^2} S(x). \quad (15)$$

$S(x)$ is defined in Eq.14 to filter out the leeward area. Here, a function $\gamma_n(x)$ is used to represent upcoming wind impact,

$$\beta_n(x, y) = \beta(x, y)\gamma_n(x, y). \quad (16)$$

To assess the reliability of each model, a residual factor is defined as following,

$$\xi = |\beta - \tau_w|, \quad (17)$$

where τ_w is the LES results. To simplify the assessing progress, the horizontal plane averaged residual value is also used here to represent the general performance of each model,

$$\xi_t = \frac{\sum_0^{L_x} \sum_0^{L_y} |\xi(x, y)|}{L_x \cdot L_y} = \frac{\sum_0^{L_x} \sum_0^{L_y} |\beta(x, y) - \tau_w(x, y)|}{L_x \cdot L_y}. \quad (18)$$

Table 1 displayed all mathematic models proposed in this work. The first model β_0 only considered dune stoss gradient effect. Assuming the linear wind profile, β_1 is proposed to certify the significance of aeolian process in sediment saltation. β_2 and β_3 includes the best fitting of wind profiles in trigonometric function formats. Considering the realistic boundary layer structures, β_4 to β_7 consider the upcoming velocity profile gradient.

Figure 3, 4 and 5 show the stress model alone with corresponding residual value distributions. Meanwhile, the average residual ξ_t results are displayed in Table 1. The mathematic model results in Figure 3 to 5 are all showing reasonable

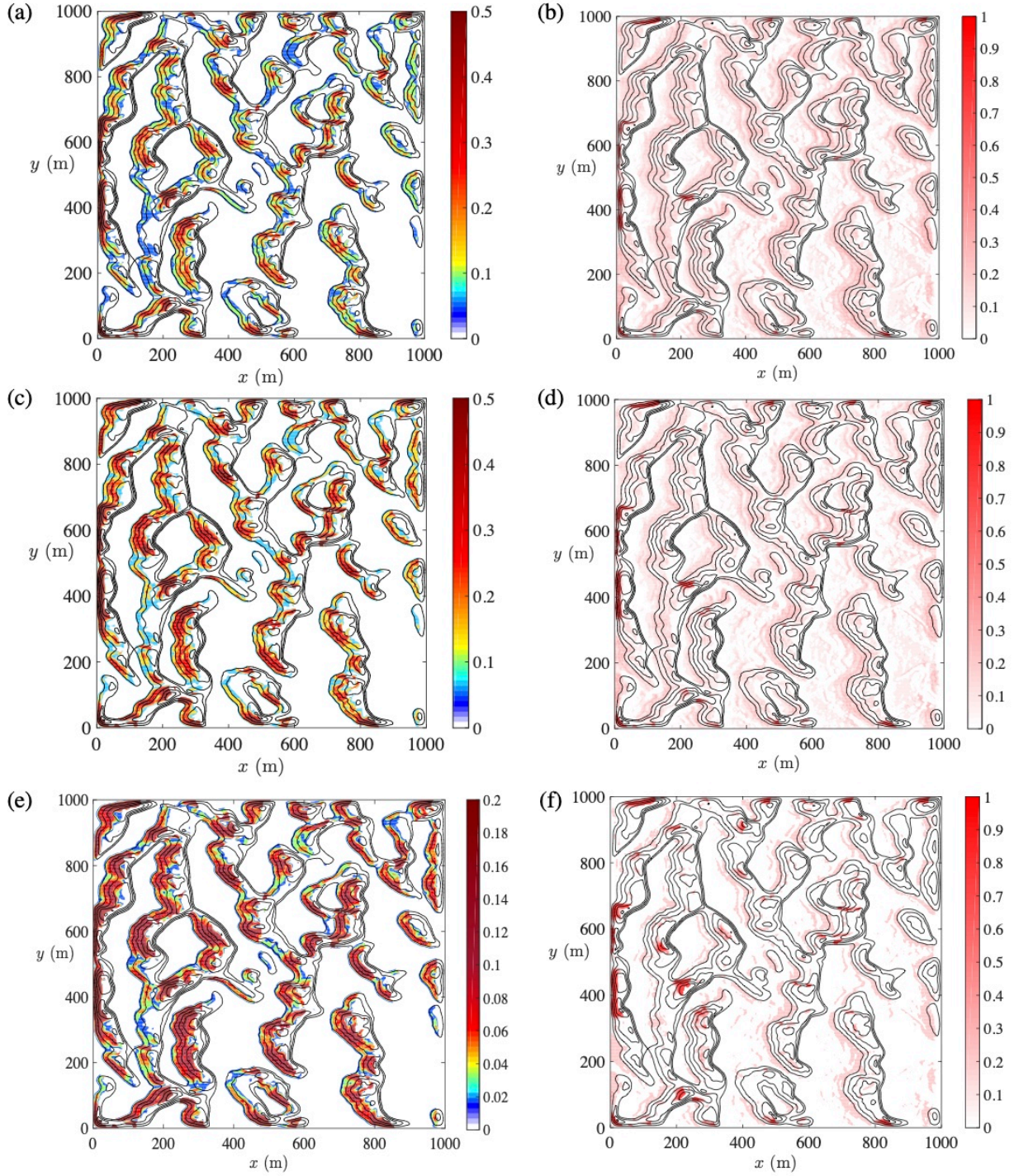


Figure 3: The author prepared the value drawn from different mathematic models: Pane (a,b) show $\beta_1(x)$ and $\xi_1(x)$; Pane (c,d) show $\beta_2(x)$ and $\xi_2(x)$; Pane (e,f) show $\beta_3(x)$ and $\xi_3(x)$ respectively.

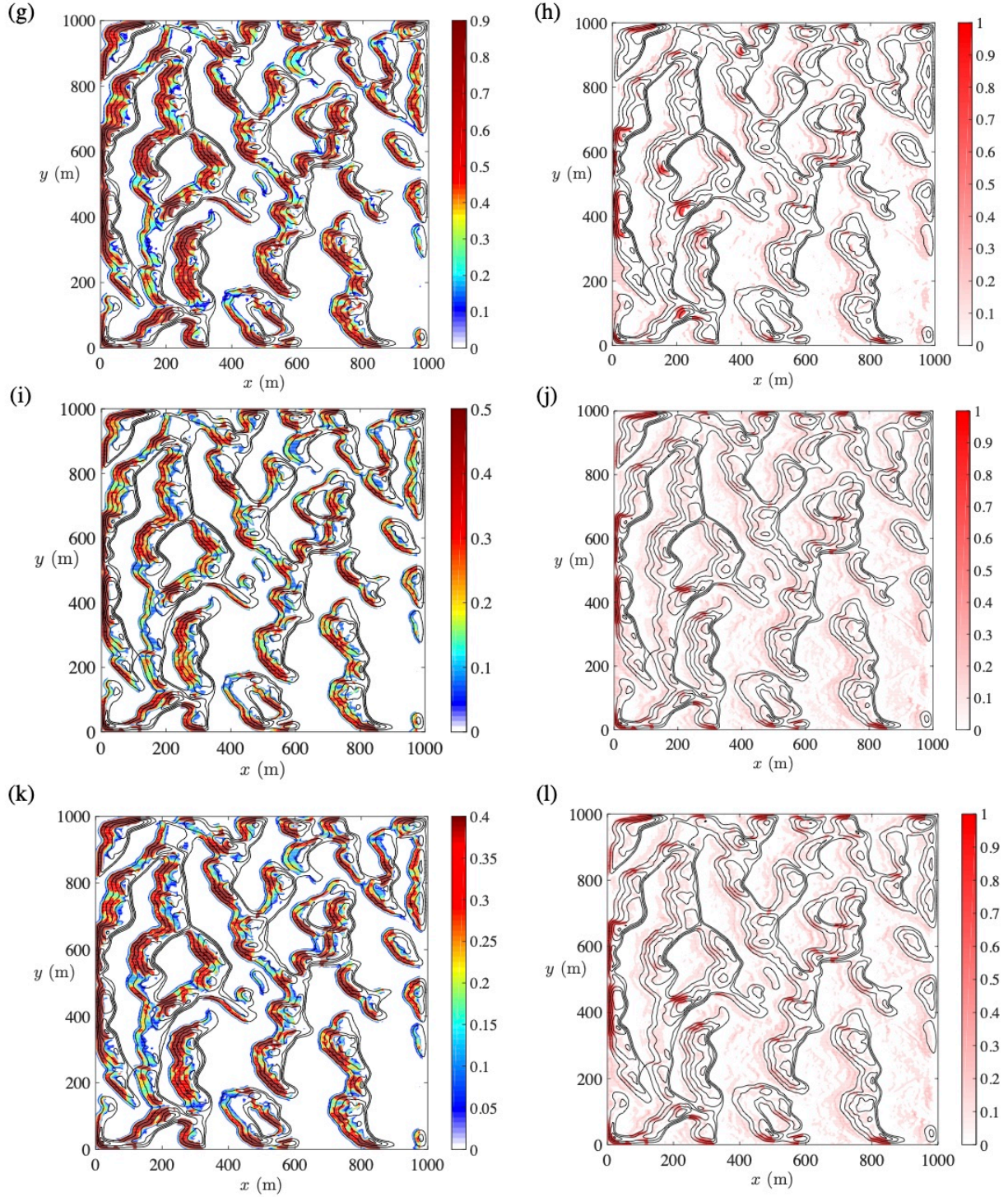


Figure 4: The author prepared the value drawn from different mathematic models: Pane (g,h) show $\beta_4(x)$ and $\xi_4(x)$; Pane (i,j) show $\beta_5(x)$ and $\xi_5(x)$; Pane (k,l) show $\beta_6(x)$ and $\xi_6(x)$ respectively.

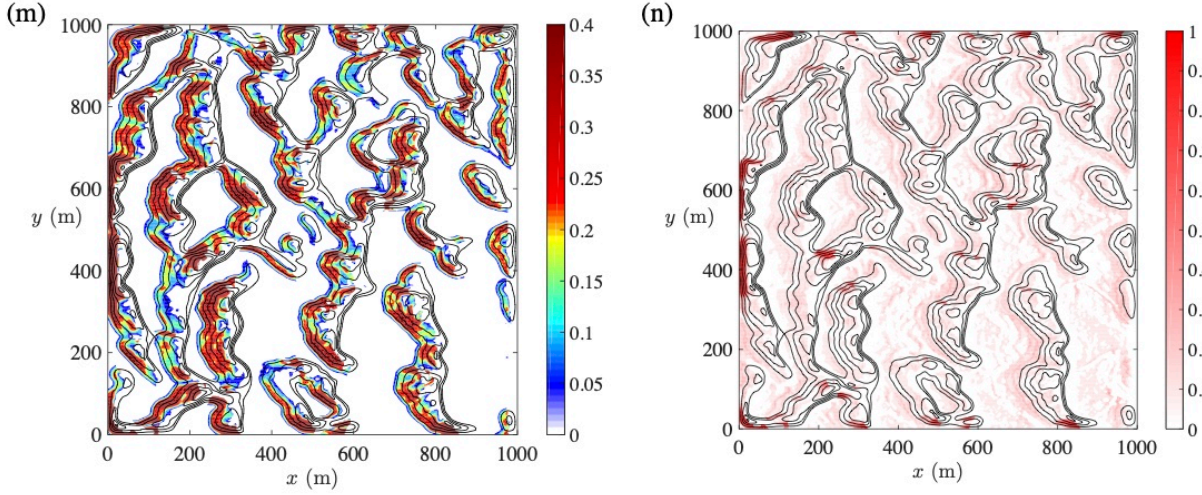


Figure 5: The author prepared the value drawn from different mathematic models: Pane (m,n) show $\beta_7(\mathbf{x})$ and $\xi_7(\mathbf{x})$ respectively.

stress magnitude and distribution. The residual distribution (f), (h) indicate β_3 , β_4 and β_5 have the best performances. From ξ_t in Table 1, the minimum value $\min(\xi_t)$ appears in β_1 , β_2 , β_5 and β_7 . Thus, based on the comprehensive assessment of residual value, β_3 and β_5 are performing the best evaluation.

In β_3 model, the mathematic model is

$$\beta_3(\mathbf{x}) = \beta(\mathbf{x})\gamma_3(\mathbf{x}) = \sqrt{\left[\frac{\partial h}{\partial x}\right]^2 + \left[\frac{\partial h}{\partial y}\right]^2} S(\mathbf{x}) \tan(h\pi/(2h_{max} \cdot k)), \quad (19)$$

where γ_3 is the best fitting of local wind profile. In β_5 , the model is

$$\beta_5(\mathbf{x}) = \beta(\mathbf{x})\gamma_5(\mathbf{x}) = \sqrt{\left[\frac{\partial h}{\partial x}\right]^2 + \left[\frac{\partial h}{\partial y}\right]^2} S(\mathbf{x}) \tanh \left[1 - \left(\frac{\frac{h}{h_{max}} - h_a}{L_s} \right)^2 \right]. \quad (20)$$

The profile of γ_5 is the gradient of theoretical boundary layer profile over dune field. According to (Wang and Anderson, 2019a; Anderson and Chamecki, 2014), boundary layer structure over dune field is composed of two regions: inertial sublayer and mixing layer. The velocity profile within inertial layer, $z > \delta_\omega$, is

$$\frac{U(z)}{u_{*,d}} = \frac{1}{\kappa} \ln \left[\frac{z}{z_0} \right], \quad (21)$$

where in mixing layer region, $0 \leq z \leq \delta_\omega$ (Wang, 2019; Wang and Cheng, 2020; Michalke, 1964; Raupach et al., 1996; Metias, 1964; Katul et al., 2002),

$$\frac{U(z)}{u_{*,d}} = \frac{U_0}{u_{*,d}} \left[1 + \tanh \left(\frac{z - h_a}{L_s} \right) \right], \quad (22)$$

Anderson and Chamecki (2014) has shown the elevated mean flow gradient in the roughness sublayer is responsible for the enhanced downward transport of high momentum fluid via turbulent sweep events. The gradient of velocity profile within inertial sublayer over dune field should be

$$\frac{dU(z)}{dz} = \frac{u_{*,d}}{\kappa z}, \quad (23)$$

but in within mixing sublayer

$$\frac{dU(z)}{dz} = \frac{U_0}{L_s} \left[1 - \left(\frac{z - h_a}{L_s} \right)^2 \right]. \quad (24)$$

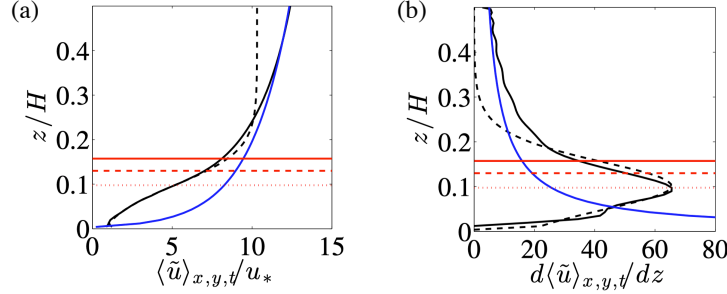


Figure 6: Panel (a), solid black line is wall-normal plane-averaged streamwise velocity of WSNM (solid black line). Dashed black line shows profile in Eq.22. Solid blue line is the profile of Eq.21. Panel (b), solid black line is vertical profile plane-averaged streamwise velocity gradient over WSNM. Dashed line shows profile in Eq.24. Solid blue line indicates the gradient profile of logarithmic wind velocity profile. Solid red line indicates the height of δ_ω . Dashed red line indicates the height of crest height h_w . Dotted red line indicates inflection height h_a .

Figure 6 shows the vertical profiles of averaged streamwise velocity and velocity gradient. In Panel (a), beneath the dotted red line, solid black line can collapse with dashed black line, which is the vertical profile of Eq.22. However, at the very high elevation, solid black line can match solid blue line, which is Eq.21. In Panel (b), the mixing layer model is still validate for velocity gradient beneath the inflection height. And at higher elevation, the flow is within inertial layer which should obey the conical logarithmic gradient profile Eq.23. Figure 6 shows vertical profile of velocity gradient and the vertical profile of wind velocity, evaluated numerically. The \tanh function has closely captured the sublayer gradient form. That the maximum gradients match is simply a result of using the velocity profiles to evaluate h_a and L_s , but the profiles also share a similar form. Similarly, we see the WSNM gradient tends towards the Eq.23 profile for $z \gtrsim \delta_\omega$. These results of the dune field sublayer are consistent with the underlying obstructed shear flow arguments (Anderson and Chamecki, 2014; Ghisalberti, 2009; Wang and Cheng, 2020; Bristow et al., 2019).

From generally global residual distributions, the locations with critical residual values show an evident consistency. These locations are defined as “channeling” regions (Wang and Anderson, 2017; Bristow et al., 2017; Wang et al., 2017; Wang and Anderson, 2018b,a, 2019a,b; Wang, 2019). Two types of perturbation are triggered due to local dune obstructions, which are illustrated through Figure 7. The first type is named “sediment scour” (Figure 7 (a)), which is spanwise rotating secondary flow keeps scouring the sediment on inner dune faces (Wang, 2019; Wang and Anderson, 2018b). The second type is “flow channeling” (Wang and Anderson, 2017). It indicates the enhancement of velocity magnitude in the narrow interdune region. Previously, Wang and Anderson (2019a) revealed the coherent structures in WSNM. That is streamwise and spanwise vortex rollers. Within mixing layer region, $z < \delta_\omega$, Kelvin-Helmholtz instability is featured in dune vortex shedding from brinklines. Spanwise vortex rollers is scaled with mixing layer length scales. Within the interdune regions, Prandtl’s secondary flow of the first and second kind keeps feeding the interdune roller evolution (Wang and Anderson, 2018b), wherein turbulent coherency is broken down into aggregations of small length scale rollers, as relative spacing decreases.

Acknowledgement

The author acknowledge Dr. William Anderson (UT Dallas) for his guidance of this work, and Dr. Gary Kocurek and Dr. David Mohrig (University of Texas at Austin) for graciously providing the LiDAR survey of the White Sands National Monument (with support from the National Park Service and the National Science Foundation), and Dr. Ken Christensen (University of Notre Dame) for sharing idealized dune DEMs. Computational resources were provided by Texas Advanced Computing Center (TACC) at the University of Texas at Austin.

References

- Albertson, J. and M. Parlange (1999). Surface length scales and shear stress: implications for land-atmosphere interaction over complex terrain. *Water Resour. Res.* 35, 2121–2132.
- Anderson, W. (2012). An immersed boundary method wall model for high-reynolds number channel flow over complex topography. *Int. J. Numer. Methods Fluids* 71, 1588–1608.

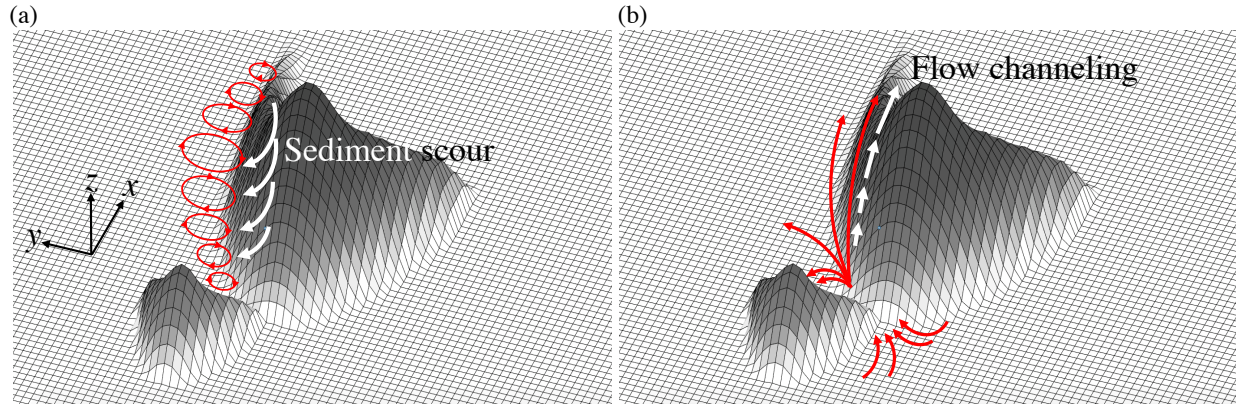


Figure 7: The schematic drawing is displayed here which has been previously published in (Wang and Anderson, 2018b). Panel (a) shows sediment scour, where red quivers indicate the rotating direction in the flow channeling region, and white quivers show sediments eroded to ground by sediment scouring. Panel (b) exhibits flow channeling effect in interdune region. Due to mass conservation, the obstructive effect of downwind dune will increase the interdune flow velocity and surface shear (Wang and Anderson, 2017). The white quivers indicate the sediment moving direction. Flow channeling enhanced surface shear triggers larger amount of sediment erosion (Wang, 2019).

- Anderson, W. (2016). Amplitude modulation of streamwise velocity fluctuations in the roughness sublayer: evidence from large-eddy simulations. *J. Fluid Mech.* 789, 567–588.
- Anderson, W. and M. Chamecki (2014). Numerical study of turbulent flow over complex aeolian dune fields: The White Sands National Monument. *Physical Review E* 89, 013005–1–14.
- Anderson, W., Q. Li, and E. Bou-Zeid (2015). Numerical simulation of flow over urban-like topographies and evaluation of turbulence temporal attributes. *J. Turbulence* 16, 809–831.
- Anderson, W. and C. Meneveau (2010). A large-eddy simulation model for boundary-layer flow over surfaces with horizontally resolved but vertically unresolved roughness elements. *Boundary-Layer Meteorol.* 137, 397–415.
- Bagnold, R. (1956). *The Physics of Blown Sand and Desert Dunes*. Chapman and Hall.
- Bou-Zeid, E., C. Meneveau, and M. Parlange (2005). A scale-dependent lagrangian dynamic model for large eddy simulation of complex turbulent flows. *Phys. Fluids* 17, 025105.
- Bristow, N., G. Blois, J. L. Best, and K. Christensen (2019). Spatial scales of turbulent flow structures associated with interacting barchan dunes. *Journal of Geophysical Research: Earth Surface* 124(5), 1175–1200.
- Bristow, N., C. Wang, G. Blois, J. Best, and K. Anderson, W. and Christensen (2017). Experimental measurements of turbulent flow structure associated with colliding barchan dunes. *Proc. 5th International Planetary Dunes Workshop, St. George, UT*.
- Ewing, R. and G. Kocurek (2010a). Aeolian dune-field pattern boundary conditions. *Geomorphology* 114, 175–187.
- Ewing, R. and G. Kocurek (2010b). Aeolian dune interactions and dune-field pattern formation: White Sands Dune Field, New Mexico. *Sedimentology* 57, 1199–1218.
- Germano, M. (1992). Turbulence: the filtering approach. *J. Fluid Mech.* 238, 325–336.
- Germano, M., U. Piomelli, P. Moin, and W. Cabot (1991). A dynamic subgrid-scale eddy viscosity model. *Phys. Fluids A* 3, 1760–1765.
- Ghisalberti, M. (2009). Obstructed shear flows: similarities across systems and scales. *J. Fluid Mech.* 641, 51.
- Hersen, P., K. Andersen, H. Elbelrhiti, B. Andreotti, P. Claudin, and S. Douady (2004). Corridors of barchan dunes: Stability and size selection. *Phys. Rev. E* 69, 011304.
- Hersen, P. and S. Douady (2005). Collision of barchan dunes as a mechanism of size regulation. *Geophys. Res. Lett.* 32, doi:10.1029/2005GL024179.
- Jerolmack, D. and D. Mohrig (2005). A unified model for subaqueous bed form dynamics. *Water Resour. Res.* 41, doi:10.1029/2005WR004329.
- Jimenez, J. (2004). Turbulent flow over rough wall. *Annu. Rev. Fluid Mech.* 36, 173.

- Katul, G., P. Wiberg, J. Albertson, and G. Hornberger (2002). A mixing layer theory for flow resistance in shallow streams. *Water Resour. Res.* 38, 32–1–8.
- Kocurek, G., M. Carr, R. Ewing, K. Havholm, Y. Nagar, and A. Singhvi (2007). White sands dune field, New Mexico: Age, dune dynamics and recent accumulations. *Sedimentary Geology* 197, 313–331.
- Kocurek, G. and R. Ewing (2005). Aeolian dune field self-organization – implications for the formation of simple versus complex dune-field patterns. *Geomorphology* 72, 94–105.
- Kok, J., E. Parteli, T. Michaels, and D. Karam (2012). The physics of wind-blown sand and dust. *Reports on Progress in Physics* 75, 106901:1–72.
- Meneveau, C. and J. Katz (2000). Scale-invariance and turbulence models for large-eddy simulation. *Annual Review of Fluid Mechanics* 32, 1–32.
- Metias, O. (1964). Direct and large eddy simulations of coherent vortices in three dimensional turbulence. In J. Bonnet (Ed.), *Eddy structure identification*, pp. 334–364. Springer-Verlag, New York.
- Michalke, A. (1964). On inviscid instability of the hyperbolic tangent velocity profile. *J. Fluid Mech.* 19, 543–556.
- Mittal, R. and G. Iaccarino (2005). Immersed boundary methods. *Annual Rev. Fluid Mech.* 37, 239–261.
- Parteli, E. J. R., V. Schwammle, H. J. Herrmann, L. H. U. Monteiro, and L. P. Maia (2006). Profile measurement and simulation of a transverse dune field in the Lençóis Maranhenses. *Geomorphology* 81, 29–42.
- Piomelli, U. and E. Balaras (2002). Wall-layer models for large-eddy simulation. *Annu. Rev. Fluid Mech.* 34, 349–374.
- Pope, S. (2000). *Turbulent flows*. Cambridge University Press.
- Raupach, M., J. Finnigan, and Y. Brunet (1996). Coherent eddies and turbulence in vegetation canopies: the mixing layer analogy. *Boundary-Layer Meteorol.* 78, 351–382.
- Shao, Y. (2008). *Physics and Modelling of Wind Erosion*. Springer Verlag.
- Tseng, Y.-H., C. Meneveau, and M. Parlange (2006). Modeling flow around bluff bodies and predicting urban dispersion using large-eddy simulation. *Environ. Sci. and Tech.* 40, 2653–2662.
- Wang, C. (2019). *Large-Eddy Simulation Study of Turbulent Flow over Dune Field*. Ph. D. thesis.
- Wang, C. and W. Anderson (2017). Numerical study of turbulent flow over stages of interacting barchan dunes: sediment scour and vorticity dynamics. In *APS Meeting Abstracts*.
- Wang, C. and W. Anderson (2018a). Large-eddy simulation of turbulent flow over spanwise-offset barchan dunes: interdune roller sustained by vortex stretching. *Bulletin of the American Physical Society* 63.
- Wang, C. and W. Anderson (2018b). Large-eddy simulation of turbulent flow over spanwise-offset barchan dunes: Interdune vortex stretching drives asymmetric erosion. *Physical Review E* 98(3), 033112.
- Wang, C. and W. Anderson (2019a). Turbulence coherence within canonical and realistic aeolian dune-field roughness sublayers. *Boundary-Layer Meteorology*.
- Wang, C. and W. Anderson (2019b). Turbulence structure over idealized and natural barchan dune fields. *Bulletin of the American Physical Society*.
- Wang, C., G. Bristow, N. Blois, K. Christensen, and W. Anderson (2017). Large-eddy simulation & experimental research of proximal deformed barchan dunes. *Proc. 5th International Planetary Dunes Workshop, St. George, UT*.
- Wang, C. and C. Cheng (2020). Turbulent characteristics within roughness sublayer over spanwise homogeneous transversal bars. *arXiv preprint arXiv:2003.06047*.
- Wang, C., Z. Tang, N. Bristow, G. Blois, K. Christensen, and W. Anderson (2016). Numerical and experimental study of flow over stages of an offset merger dune interaction. *Computers & Fluids*.